Photovoltaic Devices Employing Ternary PbS_xSe_{1-x} Nanocrystals

Wanli Ma, Joseph M. Luther, Haimei Zheng, Yue Wu, A. Paul Alivisatos*
Department of Chemistry, University of California, Berkeley
Lawrence Berkeley National Laboratory, Berkeley, CA

*Corresponding author. E-mail: alivis@berkeley.edu

We report solar cells based on highly confined nanocrystals of the ternary compound PbS_xSe_{1-x}. Crystalline, monodisperse alloyed nanocrystals are obtained using a one-pot, hot injection reaction. Rutherford back scattering and energy filtered transmission electron microscopy suggest that the S and Se anions are uniformly distributed in the alloy nanoparticles. Photovoltaic devices made using ternary nanoparticles are more efficient than either pure PbS or pure PbSe based nanocrystal devices.

Colloidal semiconductor nanocrystals display a wealth of size-dependent physical and chemical properties, including quantum confinement effects, shape dependent electronic structure,[1, 2] and control over assembly through modification of surface functionalization.[3, 4] Photovoltaic devices are an easily recognized potential application for nanocrystals due, in part, to their high photoactivity, solution processability and low cost of production. Several schemes for using nanocrystals in solar cells are under active consideration, including nanocrystal-polymer composites,[5] nanoparticle array solar cells,[6] films of partially sintered nanoparticles,[7] and nanocrystal analogues to dye-sensitized solar cells.[8] A persistent challenge for any nanoparticle-based solar cell is to take advantage of quantum confinement effects to improve the optical absorption process without overly hindering the subsequent transport of charge to the electrodes. Various

binary semiconductor nanoparticles, like CdSe, CdTe, Cu_2S, InP, and InAs, have been explored for photovoltaic devices but the reported efficiencies remain low, mostly limited by poor charge transport between the nanocrystals.[5, 7-12] With so many parameters to adjust in terms of size and shape, little work has focused on ternary or quaternary compositions of nanoparticles for solar cells. Yet it is well known from thin film solar cell studies that such compositional tuning can sometimes yield significant improvements in performance.

The Pb chalcogenide family of nanocrystals is actively investigated for nanocrystal solar cell applications because they have such large exciton Bohr radii (PbS 18 nm, PbSe 47 nm, and PbTe 150 nm). In the limit where the nanocrystals are only a tenth or so of the bulk exciton diameter, electrons and holes can tunnel through a thin organic surface coating, and therefore strong electronic coupling between particles facilitates transport of charge between nanocrystals. So far, solar cells based on binary compositions of PbSe and PbS nanocrystals have been investigated. PbSe nanocrystal solar cells generate larger short circuit photocurrents while PbS nanocrystal devices with similar bandgap have shown a larger V_{OC}.[6] This opens the possibility to better engineer particles, by creating ternary PbS_xSe_{1-x} to simultaneously optimize both carrier transport and voltage. Moreover, the properties of PbS and PbSe lead to an ideal substitutional alloy: the atomic anion radii are within 15% of each other, the lattice mismatch factor is only 2% between PbS and PbSe (see Supporting Information for the similarity of the XRD patterns), and, of course, the anions are isovalent.

Although it remains a challenge to synthesize uniform ternary PbS_xSe_{1-x} nanocrystals[13, 14] compared to the widely studied cadmium chalcogenides alloys,[15-17] we

successfully obtained monodisperse, highly crystalline nanocrystals using a one-pot, hot injection synthesis. Lead oxide (PbO, 99.999%), selenium (99.99%), oleic acid (OA, tech. grade, 90%), diphenylphosphine (DPP, 98%), 1,3-benzenedithiol (BDT, >98%), bis(trimethylsilyl) sulfide (TMS_2S, purum), 1-octadecene (ODE, 90%), anhydrous solvents and aluminum shot (99.999%) were purchased from Aldrich and used as received. Trioctylphosphine (TOP, >97%) was acquired from Strem. Nanocrystal synthesis was performed under argon atmosphere using standard air-free Schlenk line techniques. The synthesis scheme is as follows: A solution of 446mg PbO (2 mmol), 1.4 g oleic acid (5 mmol), and 10 g ODE was degassed and heated to 150^{o}C in a 50 mL three-neck flask for one hour. A mixture of proper amount 1M TOP:Se solution, TMS_2S, DPP (40mg) and ODE was then rapidly injected into this hot solution. The Se and S precursor ratio was tuned to specific values, but the total amount was kept at 1 mmol. ODE was added to dilute the precursor solution to 2 ml total. The nanocrystals were grown at 150^{o}C for 90 s, and the reaction was rapidly quenched by placing the flask in a room-temperature water bath and injecting 5 mL of anhydrous hexane. The nanocrystals were purified by precipitation twice in hexane/ethanol and once in hexane/acetone and stored in a glovebox.

Achieving and characterizing a uniformly alloyed nanocrystal remains difficult.[16] Complications arise from the difference in precursor solubility and reactivity at a given temperature, and in the difference between nucleation and growth of nanocrystals. Since TMS_2S is more reactive than TOP:Se, the stoichiometric ratio of S to Se in the resulting nanocrystal sample was greater than the injected precursor ratio. The composition of the resulting nanocrystals was characterized using energy filtered transmission electron

microscopy (EF-TEM)[18] to determine whether the nanocrystals resulted in separately nucleated PbS and PbSe, core-shell architectures, or alloyed composites. Figure 1A-C show zero loss and EF-TEM images of a sample of ~7 nm $PbS_{0.7}Se_{0.3}$ taken at the same position on a TEM grid. To achieve strong elemental signals, for EF-TEM we found it necessary to use larger nanocrystals and exchange the oleate ligands on the nanocrystal surface by adding a small amount of butylamine and washing the nanocrystals the following day. All nanocrystals in Fig. 1A (zero loss) appear in both the S mapping of Fig. 1B, and at a corresponding location in the Se mapping of Fig. 1C. The selected areas in Fig. 1A-C make the comparison easier and are shown in greater detail in Fig. 1D with the S and Se maps overlaid. The TEM results indicate that, to some extent, both Se and S are distributed inside each nanocrystal without apparent phase separation. Note that S is more prevalent than Se in the sample (i.e. $PbS_{0.7}Se_{0.3}$). Figure 1A inset shows a high-resolution TEM image of a single nanocrystal. Uniform lattice structure with no obvious stack faults or core-shell structure is observed. See Supporting Information for additional TEM images of well-packed oleate-capped ternary PbSSe nanocrystals.

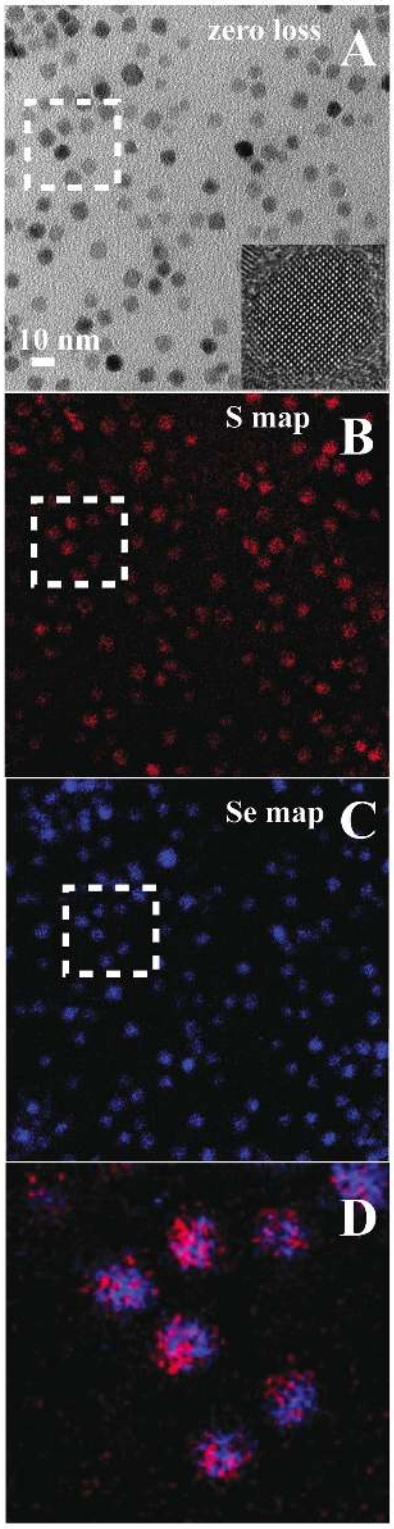

Figure 1. (A) Bright-field TEM image showing 7 nm $PbS_{0.7}Se_{0.3}$ nanocrystals. Scale bar represents 10 nm. Inset shows the high degree of crystallinity of a single ternary nanocrystal without obvious core-shell configuration. (B) Energy filtered TEM image at the same location as in (A), showing in red regions containing sulfur. (C) EF-TEM showing selenium map in blue. (D) The outlined region in (A-C) is enlarged and overlaid to show sulfur and selenium in each nanocrystal.

Rutherford backscattering spectroscopy (RBS) was then used to investigate the actual anion ratio. Figure 2 shows RBS data for a series of samples where the relative amount of S in the precursor ratio (S/(S+Se)) was systematically varied from 0 to 1. The graph shows a clear nonlinearity in the percent incorporation of anions in the nanocrystals compared to fraction present in the original precursor solution. For example: only 30% S in the precursor is needed to make nanocrystals with 70% S composition. Presumably, this nonlinearity results from the different reactivity of the chalcogen precursors. We also find that for longer reaction times, more Se is incorporated (see Fig. S5 in Supporting Information) indicating a possible radial gradient in composition; however, to be consistent, all nanocrystals used in devices were only allowed to grow for 90 seconds, thus suppressing such a gradient. RBS data shows that all samples display Pb rich composition regardless of whether or not Pb was in excess during synthesis.

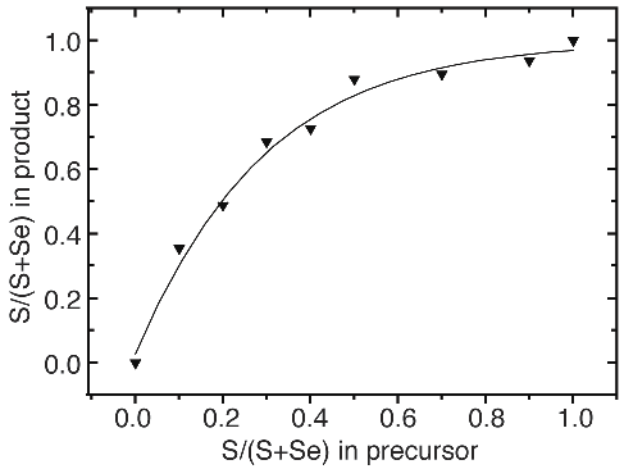

Figure 2. Rutherford back scattering data showing the relative amount of sulfur in the product versus the relative amount of sulfur in the precursor injection solution. The bowing is due to the higher reactivity of the sulfur precursor (TMS_2S) to that of the selenium precursor (TOP:Se).

For optical characterization, the alloyed nanocrystals were suspended in tetrachloroethylene. Absorbance spectra for nanocrystals with different compositions are displayed in Figure 3A. Arising from the smaller bandgap of PbSe relative to PbS for a given size,[19] we notice the red shift of the first excitation peak with reduced S composition. This trend can be observed more clearly in the inset of Fig. 3B which shows a linear relationship between the nanocrystal bandgap energy and the composition ratios. Vegard's Law predicts the structure and function of many alloyed materials: $E_{alloy} = \chi E_A + (1-\chi)E_B$, where χ is the mole fraction, E_A, E_B, and E_{alloy} are the band gap energy (or other properties) of pure composition A, pure composition B, and the alloyed material, respectively. However, this linear relationship does not apply to several classes of semiconductor alloys. For example, both bulk and nanocrystal $CdSe_xTe_{1-x}$ alloys display pronounced nonlinear "optical bowing" effects.[16, 17] Zunger and coworkers explain this type of observation by identifying three structural and electronic factors leading to nonlinearity of ternary compounds: different atomic size, electronegativity values of ions, and different lattice constants of the binary structures.[20, 21] A substantial lattice mismatch (11%) also exists between the binary semiconductors CdS and CdTe which leads to enhanced nonlinear effects there also. However, in the case of PbS_xSe_{1-x} there is only a 2% lattice mismatch between PbS and PbSe, so it is reasonable to observe less nonlinearity with composition in this alloy system, considering also that the difference in atomic size and electronegativity are the same as that for the cadmium chalcogenides. The absorbance and photoluminescence (PL) of PbS, PbSe, and $PbS_{0.7}Se_{0.3}$ nanocrystals with similar diameter are shown in Fig. 3B. The full width at half

maximum (FWHM) of PL is 188 meV, 136 meV, 122 meV for PbS, $PbS_{0.7}Se_{0.3}$ and PbSe respectively. The structured absorbance and relatively narrow PL peaks of alloyed nanocrystal indicate the sample is nearly monodisperse, which exclude the possibility of the co-existence of separate PbSe and PbS in the final synthesized nanocrystals. The uniformity of our alloyed nanocrystal structure can be further indicated by the 100 nm Stokes shift, which lies between 120 nm for PbS and 70 nm for PbSe. This result is also consistent with Vegard's Law for a true alloy.

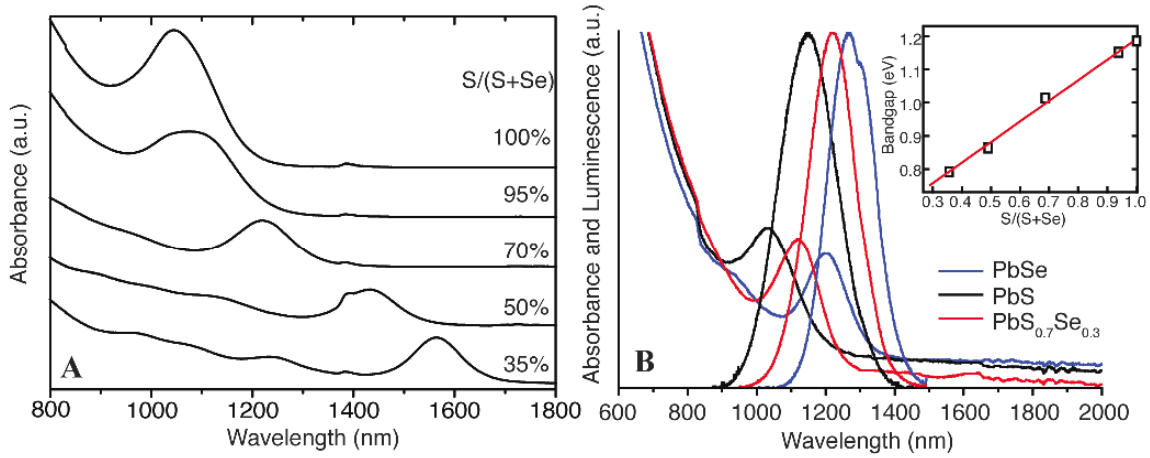

Figure 3. (A) Absorbance spectra of alloyed nanocrystals with gradually increased S concentration. All nanocrystals are ~4 nm in diameter and are grown for 90 sec. (B) Absorbance and photoluminescence of pure PbSe, pure PbS, and $PbS_{0.7}Se_{0.3}$ with similar size. The PL shows no broadening over the pure binary nanocrystals. Inset shows the variation of nanocrystals bandgap energy with different S concentrations.

We have fabricated Schottky junction back contact devices containing ternary Pb chalcogenide nanocrystals using methods reported by Nozik and coworkers for binary PbX nanocrystals.[6, 22] Briefly, patterned ITO coated glass slides were acquired from Thin Film Devices Inc (20 ± 5 ohms/sq, ITO thickness ~300 nm). The substrates were cleaned

by ultrasonication in various solvents and films of nanocrystals were deposited by sequentially dipping the substrate in a hexane solution containing the nanocrystals (~25 mg/ml) followed by dipping in a 0.01M BDT solution in acetonitrile.[23] This process was repeated such that the resulting film thickness was near 100 nm as was shown to be the optimum for PbSe devices.[24] In order to verify reproducibility of the data, three devices were made for each batch of nanocrystal with eight working pixels on each device (active area of 4 mm^2). AM1.5G illumination was obtained with a Spectra Physics Oriel 300 W Solar Simulator. The integrated intensity was set to 100 mW/cm^2 using a thermopile radiant power meter (Spectra Physics Oriel, model 70260) with fused silica window, and verified with a Hamamatsu S1787-04 diode.

Figure 4 shows the composition-dependent device performance. The *x*-axis represents composition change from pure PbSe, to pure PbS, versus various photovoltaic device parameters. Previous reports of PbS and PbSe nanocrystal devices have revealed higher V_{OC} for PbS devices but larger J_{SC} with PbSe.[6, 23, 25] Our binary PbS and PbSe results agree, but interestingly, are better in ternary PbS_xSe_{1-x} nanocrystals. The J_{SC} is mostly unaffected between S concentrations of 0 to 65%. Beyond 65% the J_{SC} rises slightly and then begins dropping at 80%. The V_{OC} is as much as double that of PbSe when using $PbS_{0.7}Se_{0.3}$.

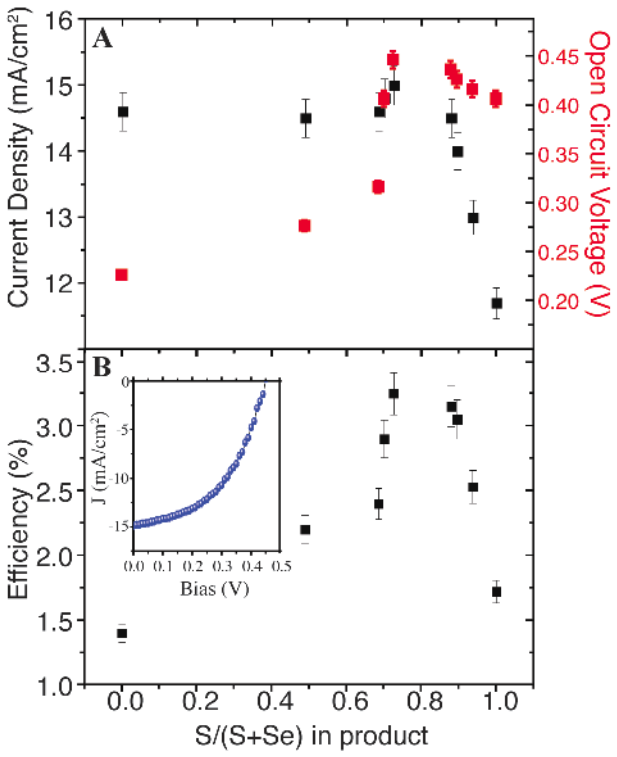

Figure 4. (A) Short circuit current density (black) and open circuit voltage (red) of solar cells made of nanocrystals with different varying S concentrations. (B) 1-sun efficiency of devices made of nanocrystals with different S concentrations. *J-V* curve of best performing solar cell device based on $PbS_{0.7}Se_{0.3}$ nanocrystals is shown in the inset of part (B). The error bars indicate the variance among 8 devices on each substrate.

As a result of both improved J_{SC} and V_{OC}, ternary PbS_xSe_{1-x} nanocrystals achieve better efficiency than pure binary nanocrystal PbSe and PbS, as shown in Fig. 4B. In fact, all devices employing ternary nanocrystals regardless of the actual anion ratio performed better than each binary control device. $PbS_{0.7}Se_{0.3}$ has the best 1-Sun power conversion efficiency of 3.3%, with a J_{SC} of 14.8 mA/cm^2, a V_{OC} of 0.45 V and a fill factor of 50%. The *J-V* curve is shown in the inset of Fig. 4B. The efficiency of devices based on pure PbS and PbSe is 1.7% and 1.4% respectively, which is consistent with previously

reported results.[6, 25] In our devices, there is a two-fold improvement for optimized alloyed nanocrystals compared to binary nanocrystals.

It has been documented that PbS and PbSe arrays of this nature have charge trapping states within the bandgap arising from ligand exchange and potentially damage during the metal deposition.[22, 26, 27] We hypothesize that the better performance of ternary nanocrystals is due to a combination of material properties as well as a redistribution of the trap states. The higher current produced by PbS_xSe_{1-x}, may arise from a significantly larger exciton Bohr radius than PbS due to the incorporation of Se (46nm for PbSe and 18nm for PbS). The larger Bohr radius delocalizes the carriers, establishing greater electronic coupling between nanocrystals, which can diminish the effects of nanocrystal surface traps and therefore facilitate charge transport. As indicated in Fig. 4A, an incorporation of ~30% Se into PbS substantially improves the current density of the cell.

PbS cells have a larger V_{OC} compared to PbSe with the same bandgap. According to Schottky junction theory, the barrier height (proportional to V_{OC}) of an ideal metal-semiconductor contact is determined by the relative position between metal work function and semiconductor Fermi energy.[28] In all devices reported here, Aluminum (work function of 4.28 eV)[29] is used as the contact and the *p*-type nanocrystal films have a Fermi level deeper than Aluminum. The size dependent conduction and valence band edge of PbS and PbSe nanocrystals have recently been measured and PbS is reported to have energy levels closer to vacuum energy than PbSe.[19] However, in practical Schottky junctions, one major limitation is that the V_{OC} cannot exceed half the bandgap. Otherwise, the minority carrier density would be larger than the majority carrier density at the junction, thus forming an inversion layer.[30] In the situation of these devices, therefore, the

true limit of the V_{OC} is governed by the difference between the intrinsic level (at mid gap) and the Fermi level of the nanocrystal film, so long as the work function of the metal contact is closer in energy to vacuum than the intrinsic energy of the semiconductor. Since the Fermi level of nanocrystals is closely related to the trap states, the density of trap states within the bandgap is most likely the cause of the differing voltages of the materials. Due to different surface energies of the binary phases to the ternary, the position and density of traps states at least at the surface in PbS, PbSe, and PbS_xSe_{1-x} may vary. This difference could determine the relative position of the Fermi level to the valence band edge of the nanocrystal film and therefore may lead to different open circuit voltages.

The combination of better J_{SC} and V_{OC} are realized in PV devices containing PbS_xSe_{1-x} nanocrystals relative to pure phase PbS and PbSe nanocrystals. S and Se compositions are closely related to the photovoltaic parameters J_{SC} and V_{OC} respectively. Alloying is demonstrated to be a successful approach to tune the composition and achieve the ternary nanocrystal with optimum photovoltaic properties. Lead chalcogenides are the only materials thus far to make high efficiency non-sintered nanocrystal solar cells because of their large exciton Bohr radius. Therefore, alloying proves to be a very simple and effective method to obtain nanocrystals with desirable bandgap, transport, and surface passivation while maintaining the advantages of the binary compound counterparts. The novel photovoltaic properties introduced by alloying derive from quantum confinement effects, and rely upon the residual nanoscale size of the components in the film. Alloying, as a methodology, may soon become an effective approach for future nanocrystal solar material engineering.

Acknowledgment. This work was supported by the Director, Office of Science, Office of Basic Energy Sciences, of the U.S. Department of Energy under Contract No. DE-AC02-05CH11231

- **DISCLAIMER**: This document was prepared as an account of work sponsored by the United States Government. While this document is believed to contain correct information, neither the United States Government nor any agency thereof, nor The Regents of the University of California, nor any of their employees, makes any warranty, express or implied, or assumes any legal responsibility for the accuracy, completeness, or usefulness of any information, apparatus, product, or process disclosed, or represents that its use would not infringe privately owned rights. Reference herein to any specific commercial product, process, or service by its trade name, trademark, manufacturer, or otherwise, does not necessarily constitute or imply its endorsement, recommendation, or favoring by the United States Government or any agency thereof, or The Regents of the University of California. The views and opinions of authors expressed herein do not necessarily state or reflect those of the United States Government or any agency thereof or The Regents of the University of California

References:

1. Manna, L.; Scher, E. C.; Alivisatos, A. P. *Journal of the American Chemical Society* **2000,** 122, (51), 12700-12706.
2. Milliron, D. J.; Hughes, S. M.; Cui, Y.; Manna, L.; Li, J. B.; Wang, L. W.; Alivisatos, A. P. *Nature* **2004,** 430, (6996), 190-195.
3. Talapin, D. V.; Yu, H.; Shevchenko, E. V.; Lobo, A.; Murray, C. B. *Journal of Physical Chemistry C* **2007,** 111, (38), 14049-14054.
4. Whaley, S. R.; English, D. S.; Hu, E. L.; Barbara, P. F.; Belcher, A. M. *Nature* **2000,** 405, (6787), 665-668.
5. Huynh, W. U.; Dittmer, J. J.; Alivisatos, A. P. *Science* **2002,** 295, (5564), 2425-2427.
6. Luther, J. M.; Law, M.; Beard, M. C.; Song, Q.; Reese, M. O.; Ellingson, R. J.; Nozik, A. J. *Nano Letters* **2008,** 8, (10), 3488-3492.
7. Gur, I.; Fromer, N. A.; Geier, M. L.; Alivisatos, A. P. *Science* **2005,** 310, (5747), 462-465.
8. Robel, I.; Subramanian, V.; Kuno, M.; Kamat, P. V. *Journal of the American Chemical Society* **2006,** 128, (7), 2385-2393.
9. Gur, I.; Fromer, N. A.; Alivisatos, A. P. *Journal of Physical Chemistry B* **2006,** 110, (50), 25543-25546.
10. Wu, Y.; Wadia, C.; Ma, W. L.; Sadtler, B.; Alivisatos, A. P. *Nano Letters* **2008,** 8, (8), 2551-2555.
11. Yu, P. R.; Zhu, K.; Norman, A. G.; Ferrere, S.; Frank, A. J.; Nozik, A. J. *Journal of Physical Chemistry B* **2006,** 110, (50), 25451-25454.
12. Zaban, A.; Micic, O. I.; Gregg, B. A.; Nozik, A. J. *Langmuir* **1998,** 14, (12), 3153-3156.
13. Brumer, M.; Kigel, A.; Amirav, L.; Sashchiuk, A.; Solomesch, O.; Tessler, N.; Lifshitz, E. *Advanced Functional Materials* **2005,** 15, (7), 1111-1116.
14. Kigel, A.; Brumer, M.; Sashchiuk, A.; Amirav, L.; Lifshitz, E. *Materials Science & Engineering C-Biomimetic and Supramolecular Systems* **2005**, 604-608.
15. Gurusinghe, N. P.; Hewa-Kasakarage, N. N.; Zamkov, M. *Journal of Physical Chemistry C* **2008,** 112, (33), 12795-12800.
16. Swafford, L. A.; Weigand, L. A.; Bowers, M. J.; McBride, J. R.; Rapaport, J. L.; Watt, T. L.; Dixit, S. K.; Feldman, L. C.; Rosenthal, S. J. *Journal of the American Chemical Society* **2006,** 128, (37), 12299-12306.
17. Bailey, R. E.; Nie, S. M. *Journal of the American Chemical Society* **2003,** 125, (23), 7100-7106.
18. Transmission electron microscopy analysis were performed using a FEI monochromated F20 UT Tecnai TEM equipped with a field emission gun, an energy loss spectrometer and a Gatan Image Filter (GIF). It was operated at 200 keV. The EFTEM images were obtained by using the three-window method.
19. Hyun, B.-R.; Zhong, Y.-W.; Bartnik, A. C.; Sun, L.; Abruna, H. D.; Wise, F. W.; Goodreau, J. D.; Matthews, J. R.; Leslie, T. M.; Borrelli, N. F. *ACS Nano* **2008,** 2, (11), 2206-2212.
20. Wei, S. H.; Zhang, S. B.; Zunger, A. *Journal of Applied Physics* **2000,** 87, (3), 1304-1311.
21. Bernard, J. E.; Zunger, A. *Physical Review B* **1987,** 36, (6), 3199-3228.
22. Luther, J. M.; Law, M.; Song, Q.; Perkins, C. L.; Beard, M. C.; Nozik, A. J. *ACS Nano* **2008,** 2, (2), 271-280.
23. Koleilat, G. I.; Levina, L.; Shukla, H.; Myrskog, S. H.; Hinds, S.; Pattantyus-Abraham, A. G.; Sargent, E. H. *ACS Nano* **2008,** 2, (5), 833-840.
24. Law, M.; Beard, M. C.; Choi, S.; Luther, J. M.; Hanna, M. C.; Nozik, A. J. *Nano Letters* **2008,** 8, (11), 3904-3910.
25. Johnston, K. W.; Pattantyus-Abraham, A. G.; Clifford, J. P.; Myrskog, S. H.; MacNeil, D. D.; Levina, L.; Sargent, E. H. *Applied Physics Letters* **2008,** 92, (15).

26. Barkhouse, D. A. R.; Pattantyus-Abraham, A. G.; Levina, L.; Sargent, E. H. *ACS Nano* **2008,** 2, (11), 2356-2362.
27. Konstantatos, G.; Levina, L.; Fischer, A.; Sargent, E. H. *Nano Letters* **2008,** 8, (5), 1446-1450.
28. Sze, S. M., *Physics of Semiconductor Devices*. 2nd ed.; John Wiley & Sons: New York, 1981.
29. Reese, M. O.; White, M. S.; Rumbles, G.; Ginley, D. S.; Shaheen, S. E. *Applied Physics Letters* **2008,** 92, (5).
30. Nelson, J., *The Physics of Solar Cells*. Imperial College Press: London, 2003.

Supporting Information for

Efficient Photovoltaic Devices Employing Ternary PbS_xSe_{1-x} Nanocrystals

Wanli Ma, Joseph M. Luther, Haimei Zheng, Yue Wu, A. Paul Alivisatos*
Department of Chemistry, University of California, Berkeley
Lawrence Berkeley National Laboratory, Berkeley, CA

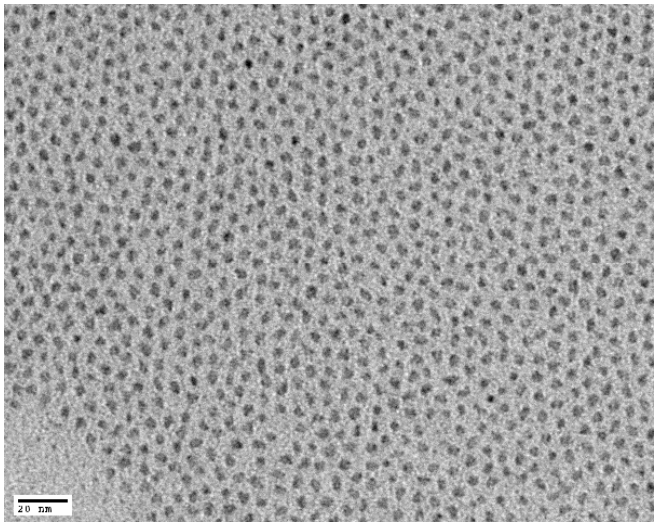

Figure S1. TEM image of typical nanocrystals employed in the high efficiency devices. S/(S+Se) = 70%.

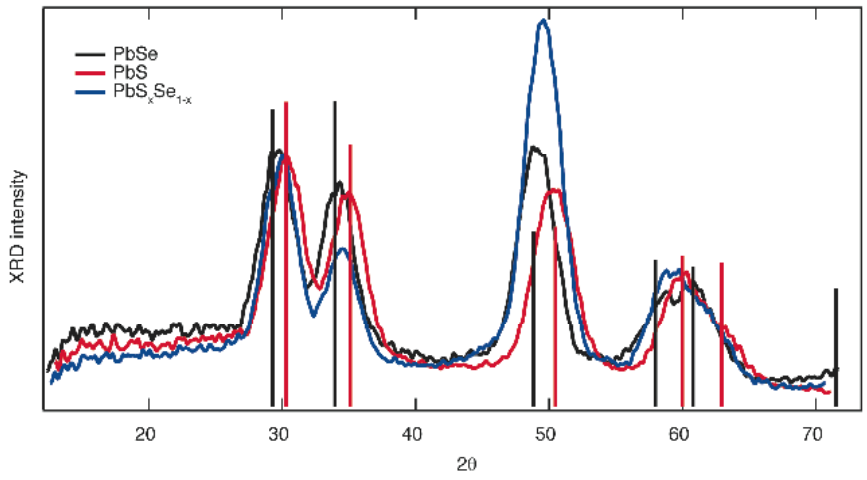

Figure S2. XRD spectrum of nanocrystals of PbS (red), PbSe (black) and PbS_xSe_{1-x} (blue). There is little shift between the peaks of PbS and PbSe. However the ternary nanocrystals peaks fall between the values of the binary nanocrystals.

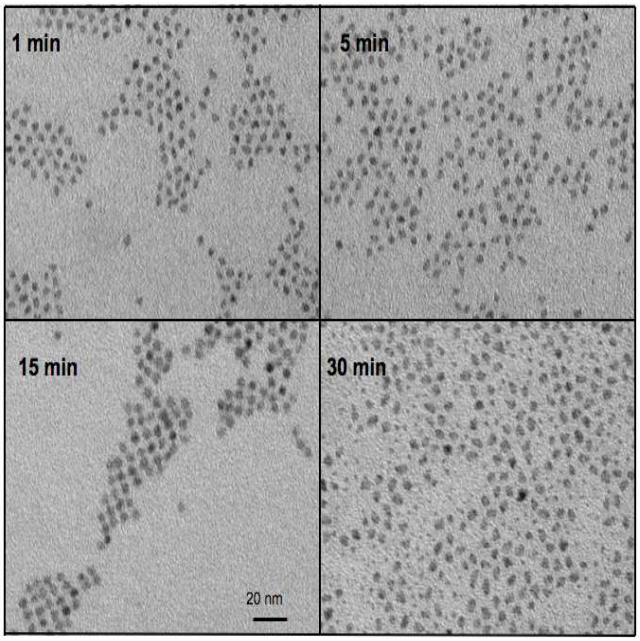

Figure S3. A synthesis for PbSSe nanocrystals was performed with timed aliquot removal to demonstrate the nanocrystal growth evolution. The best sample dispersity is seen in fast reactions. Scale bar is 20 nm for all images.

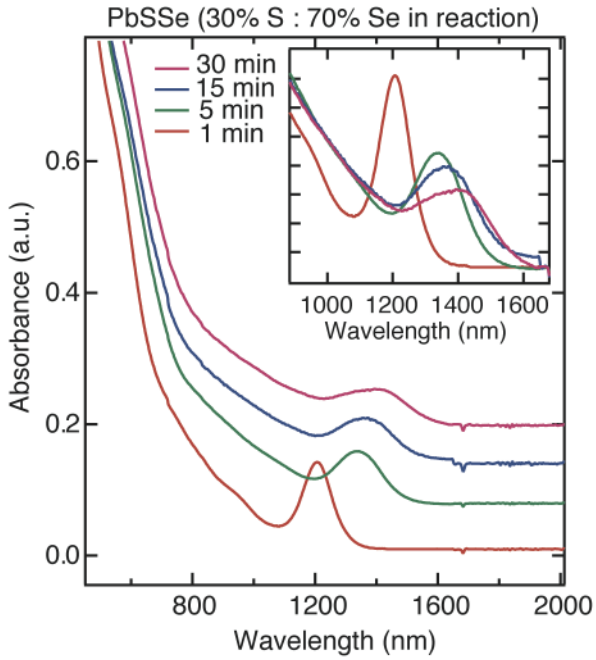

Figure S4. Absorbance of nanocrystals during the timed growth, offset for clarity. Subsequent growth times resulted in broadened first exciton peak as well as a decrease in the bandgap. Since sharpest peaks are observed at short time, a reaction time of 90 seconds was used for all device work in the manuscript.

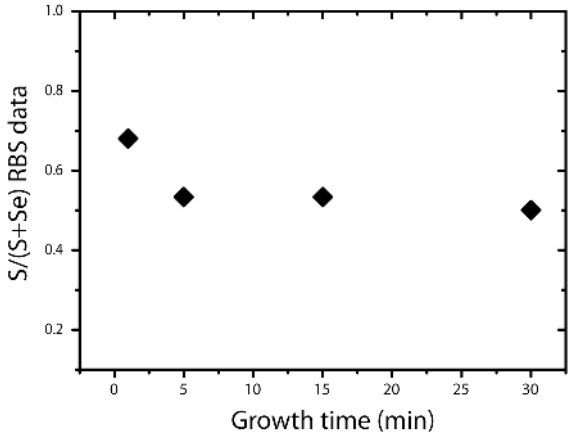

Figure S5. RBS data for the S composition of nanocrystals taken from aliquots removed at varying time after the anion precursor injection.